Alignment error calculation and measurement method of a compact spaceborne focal plane

Zhi-Peng Xue,[a,b] Sheng Wang,[a] Shan-Shan Cong,[a] Lei Zhang,[a,*] Mei-Jiao Sun,[a] Chun-Yu Zhu,[a] Chang Liu,[a] and Hang Liu[a]
[a]Chang Guang Satellite Technology Company, Changchun, China
[b]Chinese Academy of Sciences, Changchun Institute of Optics, Fine Mechanics, and Physics, Changchun, China

Abstract. The thermal and mechanical stabilization of the focal plane assembly (FPA) naturally has a magnificent impact on the performance of space camera. Thermal and mechanical features of the proposed FPA are described first. Special attention is paid to the thermo-structure design of the FPA. Then the fitting methods based on singular value decomposition and least square are proposed to use the finite-element analysis results to predict the relative position changes between charge coupled devices under thermal and mechanical load cases. A comprehensive finite-element model of the FPA has been built, and the alignment errors, which were induced thermal and gravity loads, are predicted based on the proposed fitting method. To further prove that the design of FPA meets the mechanical and thermal stability requirements, an optical bench was developed. Meanwhile thermal cycling and vibration test of the three FPAs were performed; the alignment error measurements of the FPAs after each test were also performed. Both the simulation and tests show a good stability of the FPA design under operational and test environments. © *2021 Society of Photo-Optical Instrumentation Engineers (SPIE)* [DOI: 10.1117/1.JATIS.7.4.044002]

Keywords: focal plane assembly; optical splicing; finite-element analysis; fitting; singular value decomposition.

Paper 21047 received Apr. 26, 2021; accepted for publication Sep. 10, 2021; published online Nov. 18, 2021.

1 Introduction

Focal plane system is an important component of space remote sensing camera, which generally includes focal plane assembly (FPA), focal plane modules, and focal plane electronics. The resolution of the imaging sensor directly determines the field-of-view angle of the space camera. In order to meet the requirement of wide swath with high spatial under the limitation of a number of pixels of current sensors, one method is to design the FPA by mechanical mosaic.[1] The FPA of the high-resolution imaging science experiment (HIRISE) camera, which was developed by the U.S.A NAVA consists of the 14 charge coupled devices (CCDs) mounted on carriers by mechanical staggered lap design. Li et al.[2] introduced the characters of the HIRISE FPA in terms of the structural layout, material selection, and mechanical splicing of the CCD. Malone et al.[3] introduced the thermal, optical, mechanical, and structural features of the Operational Land Imager 2's FPA. All 14 of the CCDs were aligned to better than 7.0 μm ($X - Y$) and were co-planar to 9.5 μm based on a combination of precisely machined parts and active alignment using a highly accurate video microscope and a 6-axis micropositioner.[4] They also performed vibration and thermal cycle testing of the FPA to verify the design meets the vibration and thermal stability requirements.

The problem with the CCD mosaic solution is that no matter how close the two sensors are there will always be a gap. The gaps cause discontinuities in the image detected, resulting in poor image detection. Another method is optical splicing, which uses optical components such as flat mirror to divide the image field into separate segments, which are then imaged on the individual

*Address all correspondence to Lei Zhang, 18686344285@163.com

2329-4124/2021/$28.00 © 2021 SPIE

sensor's sensitive area.[5] This method can ensure that the same spectral segment of each sensor can be imaged at the same time. Pranyies et al.[6] introduced the optical butting technique used in PLEIADES FPA and performed a simulation considering for a worst-case assumption of 12-min exposure period to study the dimensional stability and thermal behavior. A more detailed description of PLEIADES FPA's optical architecture can be found in Ref. 7 where the ground support equipment for integrating and measuring of the FPA was also introduced.

The development of an FPA in a space camera typically involves a period of design, fabrication, assembly, and testing to ensure relatively high stability and precision.[8] Many scholars have studied and introduced the design factors, material selection, and module division of focal plane structure design considering the requirements of mechanical and thermal stability.[9] Thermal effects are the primary cause for alignment drift during exposure period. Hamill[10] discussed the temperature effects on optical components and their surrounding structure such as a loss of image and beam quality. The focal plane simulations were mainly based on the finite-element analysis (FEA) methods[11] to provide accurate and fidelity mechanical response prediction. A detailed finite-element model has been built for modal, static, and dynamics analyses of the FPA of near-infrared spectrophotometer.[12] Sultana and Neill[13] developed a detailed finite-element model of the CCD array and the mount to determine the worst-case out-of-plane displacements due to thermal and gravity loadings. They also conducted a series of holographic interferometry experiments to verify the accuracy of the finite-element model. However, the current FEA methods are still focused on the prediction of mechanical response, and there is no further analysis of the effect of structural deformation on focal plane alignment error.

Many structural-thermal-optical integrated methods have been developed in the past years to provide insight into the interdisciplinary design relationships of thermal and structural designs and their impact through a deterministic assessment of optical performance.[14,15] The FE displacement results for an optical surface were often decomposed into average surface rigid motion and higher order distortions, which are represented by polynomials and/or grid arrays.[16] However, there are few studies on how to use the finite-element displacement results to fit the relative position changes between sensors so as to analyze the impact of thermal and gravity loadings on the alignment error. In recent years, the use of singular value decomposition (SVD) to approximate a surface or plane fitting was carried out.[17] Zermas et al.[18] fitted the ground plane based on SVD method using the 3D point cloud that is provided by modern LiDAR sensor.

The important issues for the FPA are the alignment accuracy and stability. The high alignment accuracy is achieved by the precision FPA integration, and the alignment stability should be maintained during the entire operational lifetime of the satellite. In summary, the events that could negatively influence the alignment accuracy and stability of the FPA, are as follows.

(1) The initial positional error of the CCD and mirror.
(2) The misalignment caused by the structural deformation due to the different thermal and gravity conditions such as ground alignment and in orbit environment.
(3) The additional misalignment after thermal cycle and vibration test.

In this paper, the effect of structural deformation due to thermal and mechanical loads caused by different environments on the focal plane alignment error is analytically studied. Moreover, we proposed an optical bench setup for the integration and measurement of the PFA. We also performed vibration and thermal cycle testing of the FPA to verify its vibration and thermal stability. In order to calculate the relative position changes of each CCDs, we proposed a fitting method for the CCD sensitive area and mirror surface plane based on SVD. The focus remains on the following aspects.

(1) A detailed description of the fitting of the CCDs and mirror using FEA results is given to show how the alignment error of FPA under thermal and mechanical load cases can be easily and effectively predicted.
(2) Show that how to implement the proposed method to the analysis of a FPA with 3 CCDs and a mirror.
(3) Describe how to study the mechanical and thermal stability of the FPA.

In the next section, the design of the FPA studied in this paper is described. In Sec. 3, kinematics of infinitesimal deformation is investigated first to obtain the relationship between nodal displacement and thermal strain. Then both plane and line fitting methods are proposed to predict the change of relative positions of CCD sensitive areas. Section 4 performs a thermostructure analysis of the FPA, and the results were postprocessed to calculate the alignment error under thermal load case. Section 5 presents the measurement method and test of three FPAs followed by conclusions in Sec. 6.

2 Design of FPA

2.1 *Optical Splicing System*

In our design, the FPA consists of 3 CCDs and each CCD has 6496×5 pixels ($4.5\ \mu\mathrm{m} \times 4.5\ \mu\mathrm{m}$ pixel size). As shown in Fig. 1(a), a flat mirror folds the optical paths toward to CCD 2. The mirror surface has an inclined angle of 45 deg in relation to the optical axis so that the mapped focal plane is parallel to the optical axis, which is easy to locate CCD 2. The layout of CCD sensitive areas is depicted in Fig. 1(b). The FPA's co-planarity requirement is ± 0.01 mm, and the alignment requirements in the cross-track and along-track direction are ± 0.005 and ± 0.002 mm, respectively.

2.2 *Thermo-Structure Design*

One of the main design requirements is to keep the alignment accuracy of the focal plane in a wide temperature range. The silicon carbide/aluminum composite (SiC/Al) material has been chosen for the main parts of the FPA structure including the substrate and TDICCD structure. A very good thermal conductance, a very low-thermal expansion coefficient and a high stiffness are simultaneously offered by this material. Moreover, its linear expansion coefficient matches with the CCD's package, which makes the FPA be with good thermal conductivity and temperature stability.

The structure of FPA is shown in Fig. 2, and three CCDs, one mirror, and a thermal storage device are bolted on the focal plane substrate. The dimensions of the FPA are $167 \times 105 \times 91$ mm. For the substrate provides the benchmark of integration and optical axis calibration, it is designed rigidity and stability with a reasonable mass budget. The screws are evenly arranged around the substrate to make the thermal center of FPA approximately located in the geometric center. The advantages of this design will be discussed in Sec. 4 in combination with the thermo-structure analysis results.

In order to obtain the stability of the FPA, the simulation is performed considering the requirements to keep the alignment precision of the focal plane in room temperature and operating temperature in orbit. The experiment is performed considering the requirements to keep the alignment precision of the focal plane before and after thermal and vibration loads.

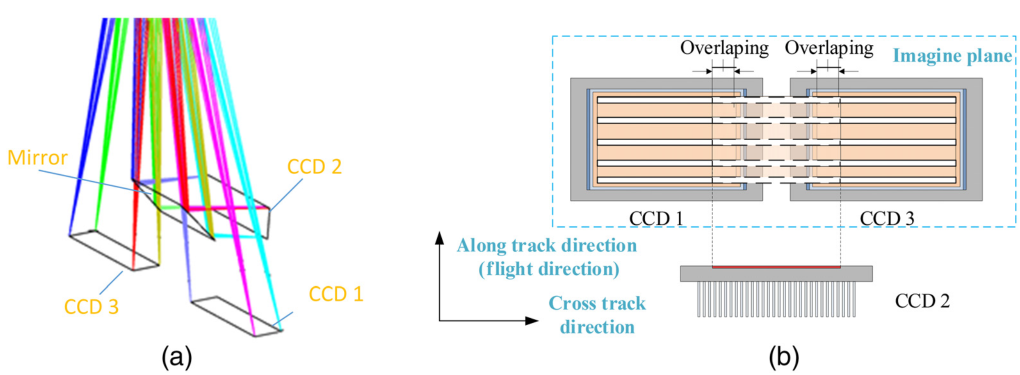

Fig. 1 The optical butting system: (a) block diagram of image measuring system and (b) the CCD layout in FPA.

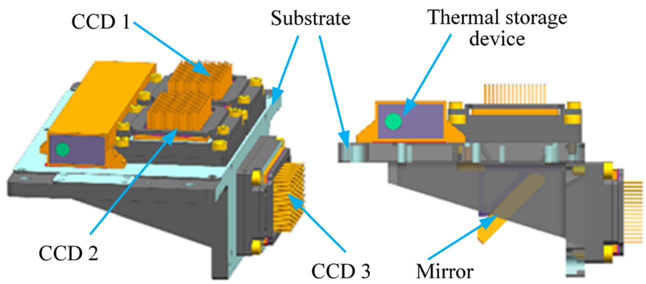

Fig. 2 FPA overall views.

3 Alignment Error Modeling Method

The change of the temperature of FPA will cause the thermal strain of the structure, resulting in the changes of the size and position of each part of the focal plane, which leads to the decline of the alignment accuracy. In finite-element method, thermal deformations are essentially the relative displacements of finite-element nodes caused by thermal load, which leads to the change of the shape of the continuous deformable body. The kinematic of infinitesimal deformation is introduced first to show the relationship between deformation and strain. Then the data post-processing method using the finite-element nodal position and displacement is presented to predict the alignment error caused by the thermal or mechanical loads.

3.1 *Kinematics of Infinitesimal Deformation*

As shown in Fig. 3, B_0 is the shape domain of the finite-element model without any deformation. After deformation, the shape domain becomes B. The position of node P_0 is denoted by vector $\boldsymbol{h}$ in the undeformed state. Node P_0 moves to a new position $\boldsymbol{r}$ due to a displacement vector $\boldsymbol{u}$. Then the vector $\boldsymbol{r}$ is denoted as

$$\boldsymbol{r} = \boldsymbol{h} + \boldsymbol{u}, \tag{1}$$

where $\boldsymbol{h} = [x, y, z]^{\mathrm{T}}$, and the displacement vector $\boldsymbol{u} = [u_x, u_y, u_z]^{\mathrm{T}}$.

Differentiating both side of the above equation with respect to $\boldsymbol{h}$ as

$$dr = (I + \nabla u)dh, \tag{2}$$

∇u is the gradient of the displacement vector and can be written as

$$\nabla u = \begin{bmatrix} \varepsilon_{xx} & \varepsilon_{xy} & \varepsilon_{xz} \\ \varepsilon_{yx} & \varepsilon_{yy} & \varepsilon_{yz} \\ \varepsilon_{zx} & \varepsilon_{zy} & \varepsilon_{zz} \end{bmatrix}, \tag{3}$$

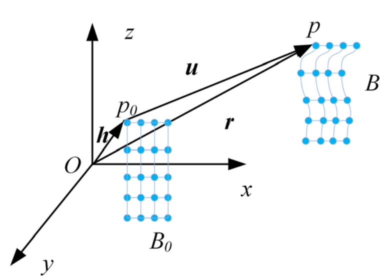

Fig. 3 Kinematics of infinitesimal deformation.

in which

$$\varepsilon_{ij} = \frac{\partial u_i}{\partial h_j}, \tag{4}$$

where i and j represent coordinates x, y, or z.

According to the generalized Hooke's law, the linear strains ε_{xx}, ε_{yy}, and ε_{zz} are given by

$$\begin{cases} \varepsilon_{xx} = \frac{1}{E}[\sigma_x - \mu(\sigma_y + \sigma_z)] + \alpha\Delta t \\ \varepsilon_{yy} = \frac{1}{E}[\sigma_y - \mu(\sigma_z + \sigma_x)] + \alpha\Delta t \\ \varepsilon_{zz} = \frac{1}{E}[\sigma_z - \mu(\sigma_x + \sigma_y)] + \alpha\Delta t \end{cases}, \tag{5}$$

where E is the modulus of elasticity, μ is the Poisson's ratio, σ is the stress, α is the coefficient of linear expansion, and Δt is the temperature change value.

3.2 *Alignment Error Calculation*

3.2.1 *Fitting method*

The displaced nodal positions (x_i, y_i, z_i) are used to fit the new planes of the mirror and CCD sensitive areas. For the estimation of the plane, the linear mode is utilized as

$$ax_i + by_i + cz_i = d. \tag{6}$$

Then we obtain

$$a\overline{x} + b\overline{y} + c\overline{z} = d, \tag{7}$$

where (a, b, c) is the normal unit vector of the plane, and d is the perpendicular distance between the coordinates system origin and the plane. $\overline{x}$, $\overline{y}$, $\overline{z}$ are the mean values of x_i, y_i, and z_i. Eq. (6) minus Eq. (7), we obtain

$$a(x_i - \overline{x}) + b(y_i - \overline{y}) + c(z_i - \overline{z}) = 0. \tag{8}$$

Equation (8) can be written in the form of a matrix:

$$AX = 0, \tag{9}$$

$$A = \begin{bmatrix} x_1 - \overline{x} & y_1 - \overline{y} & z_1 - \overline{z} \\ x_2 - \overline{x} & y_2 - \overline{y} & z_2 - \overline{z} \\ & \cdots & \\ x_n - \overline{x} & y_n - \overline{y} & z_n - \overline{z} \end{bmatrix}, \tag{10}$$

in which $A \in R^{m*3}$, m is the number of finite-element nodes, and $m > 3$, $X = [a, b, c]^{\mathrm{T}}$ represents the normal vector of the fitted plane. Because Eq. (9) is homogeneous, a constraint condition is set to avoid the $X = 0$ result as

$$\|X\| = a^2 + b^2 + c^2 = 1. \tag{11}$$

The purpose of fitting is to make the sum of the distances between the fitted plane and all nodes as small as possible. Then the objective function is

$$\min_{\|X=1\|} \|AX\|. \tag{12}$$

The singular decomposition A is

$$A = U\Sigma V^{\mathrm{T}} = U \begin{bmatrix} \lambda_1 & & \\ & \lambda_2 & \\ & & \lambda_3 \end{bmatrix} V^{\mathrm{T}}, \tag{13}$$

where $U \in R^{m*m}$ and $V \in R^{3*3}$ are orthogonal matrices, and $\Sigma \in R^{3*3}$ is a diagonal matrix containing the singular value $\lambda_1 \geq \lambda_2 \geq \lambda_3$ (λ_1^2, λ_2^2, and λ_3^2 are the eigenvalue of $A^{\mathrm{T}}A$).

We have

$$\min \|AX\| = \min(X^{\mathrm{T}}A^{\mathrm{T}}AX) = \lambda_{\min}^2. \tag{14}$$

The detailed derivation process is presented in Appendix A. The minimal value of $\|AX\|$ is λ_3^2, then the eigenvector of $A^{\mathrm{T}}A$ corresponding to the minimum eigenvalue is the optimal solution:

$$A^{\mathrm{T}}A = (U\Sigma V^{\mathrm{T}})^{\mathrm{T}}(U\Sigma V^{\mathrm{T}}) = V\Sigma^{\mathrm{T}}\Sigma V^{\mathrm{T}}. \tag{15}$$

It can be seen in Eq. (14) that the eigenvector of $A^{\mathrm{T}}A$ is the column vector of V. Therefore, X is the row vector of V corresponding to the minimum eigenvalue of A. Then d is directly calculated from Eq. (7).

The mirror's fitted plane is used to map the displaced nodes of CCD 2 to imaging positions (x_s, y_s, z_s) as follows:

$$\begin{cases} x_s = x - 2a(ax + by + cz + d)/\sqrt{a^2 + b^2 + c^2} \\ y_s = y - 2b(ax + by + cz + d)/\sqrt{a^2 + b^2 + c^2}. \\ z_s = z - 2c(ax + by + cz + d)/\sqrt{a^2 + b^2 + c^2} \end{cases} \tag{16}$$

For line fitting, the fitted line can be defined with the following equation:

$$y_i = a_l x_i + b_l. \tag{17}$$

The least square method is used as

$$e^2 = \sum_{i=1}^{n} (y_i - (a_l x_i + b_l))^2. \tag{18}$$

The partial derivatives of function e for a_l and b_l are obtained, respectively. Then a_l and b_l can be obtained by follows:

$$\begin{pmatrix} \sum_{i=1}^{n} x_i^2 & \sum_{i=1}^{n} x_i \\ \sum_{i=1}^{n} x_i & n \end{pmatrix} \begin{pmatrix} a_l \\ b_l \end{pmatrix} = \begin{pmatrix} \sum_{i=1}^{n} y_i x_i \\ \sum_{i=1}^{n} y_i \end{pmatrix}. \tag{19}$$

3.2.2 *Alignment error*

The co-planarity error of the three CCDs is represented by the root mean square (RMS) of the distance offset between the displaced nodal positions and the fitted plane. The distance is calculated as

$$D_{\text{plane}}^i = (ax_i + by_i + cz_i + d)/\sqrt{a^2 + b^2 + c^2}. \tag{20}$$

The rectilinearity error (position error in the along-track direction) is also calculated by the RMS of the distance offset between the displaced nodal positions and the fitted line. The distance is calculated as

$$D_{\text{line}}^i = (a_l x_i - y_i + b_l)/\sqrt{a_l^2 + b_l^2}. \tag{21}$$

To predict the lap dimension changes, the average of the displacements in X direction of each CCD is calculated. Then the relative distance changes are calculated as

$$D_{\text{lap}}^{ij} = \overline{d_j^x} - \overline{d_i^x}, \tag{22}$$

where D_{lap}^{ij} is the X directional distance changes between CCD i and j; $\overline{d^x}$ is the average displacement of the CCD in X direction; $i = 1$ or 2 and $j = i + 1$.

4 Thermo-Structure Analysis and Postprocessing

In this section, the thermo-structure analysis of the FPA is performed and the results are postprocessed by the proposed method. We define the nodes after deformation as displaced nodes and the nodes after mapped by mirror as mapped nodes. The main process includes the following.

(1) The finite-element model of FPA is established and analyzed.
(2) The finite-element nodes used for data postprocessing of the mirror and CCDs are selected. The positions and displacements of these nodes are used to calculated the new positions after thermal deformation according to Eq. (1).
(3) A new mirror plane is fitted using the displaced nodes of mirror. Then the displaced nodes of CCD 2 are mapped to new positions by the fitted mirror plane.
(4) The displaced nodes of CCD 1 and 3 and the mapped nodes of CCD 2 are used to fit imaging plane. Then the RMS value of the distances between these nodes and the fitted imaging plane is calculated to predict the coplanar accuracy.
(5) The displaced nodes of CCD 1 and 3 and the mapped nodes of CCD 2, which are in the same row, are selected for line fitting. Then the RMS value of the distances between these nodes and the fitted line is calculated to predict the position accuracy.

4.1 *Thermo-Structure Analysis*

A detailed finite-element model of the FPA was constructed as shown in Fig. 4. Hexahedral elements were used to construct the finite-element model. The substrate consists of four $\varphi 4.2$ holes for M4 bolts, and the interface nodes of these four holes are constrained in 6 degrees of freedom as shown in Fig. 4. Then both sides of the substrate are constrained and other boundaries were allowed to expand freely. Our response of interest is the displacements of the nodes on the CCDs as shown in Fig. 5. To ensure the FEA model captures the system behavior while reducing solves time, we have compared the results of different FEA model complexities. Then 10,287 elements are used to construct the FEA model and additional elements refinement does not affect results. The X, Y, and Z directions in the model are the cross-track, along-track, and optical-axis direction, respectively. The nodes selected for data postprocessing are illustrated in Fig. 5, all nodes on the plane of the flat mirror are selected, and two rows (9 nodes per row) in the upper and lower of each CCD's sensitive area are selected.

An FEA was performed on the FPA. Considering the requirements to keep the alignment accuracy of the focal plane in room temperature (alignment temperature) and operating temperature in orbit, a worst case assumption of an isothermal change of $+10°C$ is given for the CCD

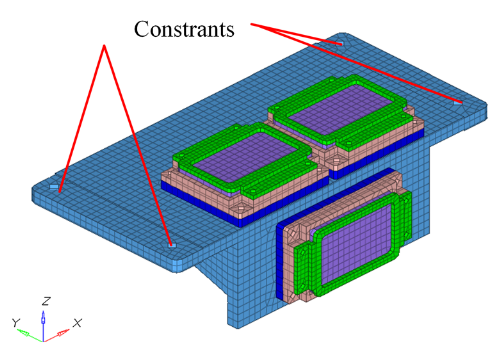

Fig. 4 Finite-element model of FPA.

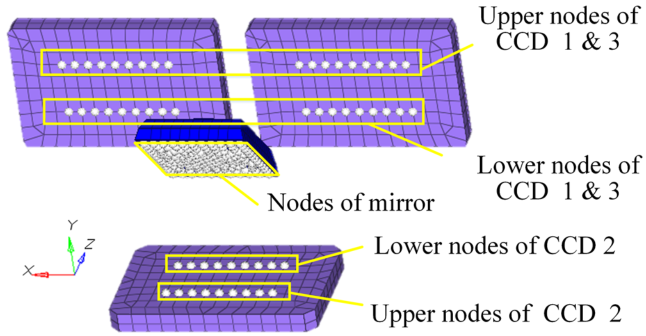

Fig. 5 Nodes selected for postprocessing.

substrate would be controlled to 25°C to 30°C during flight and the room temperature is 20°C. The FPA was subject to gravity in Z direction and an isothermal change of $+10$°C (from 20°C to 30°C). The resulting displacement contour map is shown in Fig. 6(a). It can be seen that due to the symmetrical design of thermal structure, the thermal center is approximately located at the geometric center of the focal plane. Then the deformations of the CCD sensitive areas are very small and uniform, which are helpful to ensure the alignment accuracy of the CCDs.

Contours of displacements in X, Y, and Z directions are also shown in Fig. 6. The deformations in X direction will affect the lapping accuracy of the CCDs. The deformations in Y direction reduce the positional accuracy of CCD 1 and 3 in the along-track dimension. The Y directional displacements of the nodes of CCD 2 cause a rigid-body displacement of CCD 2 in Y direction for these nodes have the same distance to the Y directional thermal center. After mapped by mirror, the Y directional rigid-body displacement of CCD 2 becomes the offset

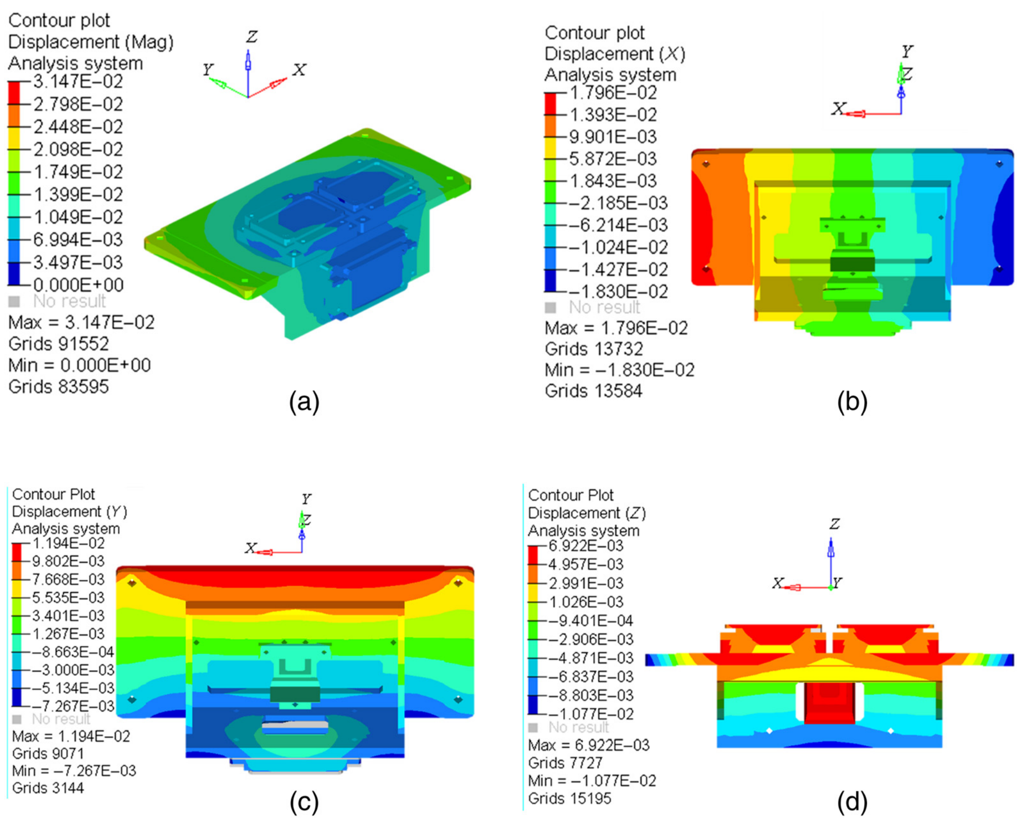

Fig. 6 Contours of displacements in X, Y, and Z directions. (a) FE displacement contour map, (b) displacement contour map in X direction, (c) displacement contour map in Y direction, and (d) displacement contour map in Z direction.

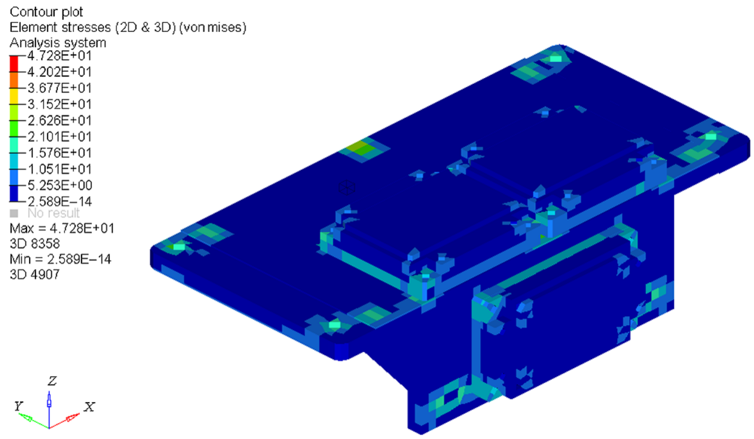

Fig. 7 Stress contour.

in Z direction of imaging plane, which reduces the coplanar accuracy. Similarly, the deformations in Z direction affect the coplanar accuracy of CCD 1 and 3, and the positioning accuracy of CCD 2 in the along-track dimension.

The stress contour in the thermal elastic analysis is shown in Fig. 7. The max von-Mises stress under the static condition have been evaluated to be around 47 MPa, which gives a margin of safety (MS) of 149% considering a structure made in SiC/Al (microyield strength 117 MPa and MS $= \sigma_{\text{allow}}/\sigma_{\text{peak}} - 1.0$). The stress levels in the CCDs are kept below the microyield strength to avoid the permanent strain (plastic deformation on the order of 10^{-6} m deformation/m) to maintain precision alignment. Therefore, the FPA offers a high stability.

4.2 *Data Postprocessing*

First, the new positions after deformation of the selected nodes as shown in Fig. 5 were calculated by the sum of the displacements and undeformed positions according to Eq. (1). The displaced nodes of the mirror were used to fit the new mirror plane. Then the displaced nodes of CCD 2 were mapped to new positions through the fitted plane of the mirror. The fitted plane of the mirror, the displaced and mapped nodes of CCD 2, and the displaced nodes of CCD 1 and 3 are shown in Fig. 8.

For co-planarity error prediction, the displaced nodes of CCD 1 and 3 and the mapped nodes of CCD 2 were used to fit the imaging plane as shown in Fig. 9. A relative high co-planarity accuracy can be observed between the displaced nodes of CCD 1 and 3. However, there is an obvious offset between the mapped nodes of CCD 2 and the displaced nodes of CCD 1 and 3. This is mainly caused by the rigid-body displacement of CCD 2 in Y direction as discussed in Sec. 4.1. Then the displaced nodes of CCD 1 and 3 are used for plane fitting, and the distances

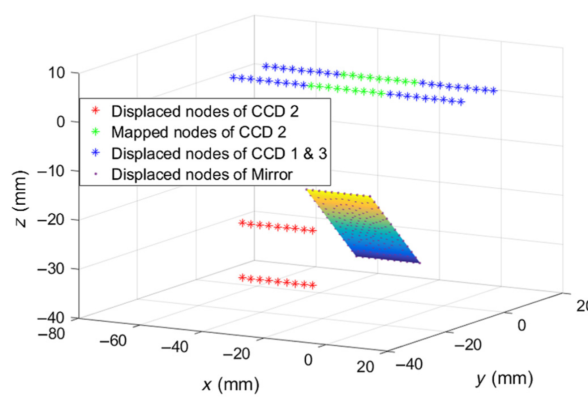

Fig. 8 Nodes and plane of the FPA.

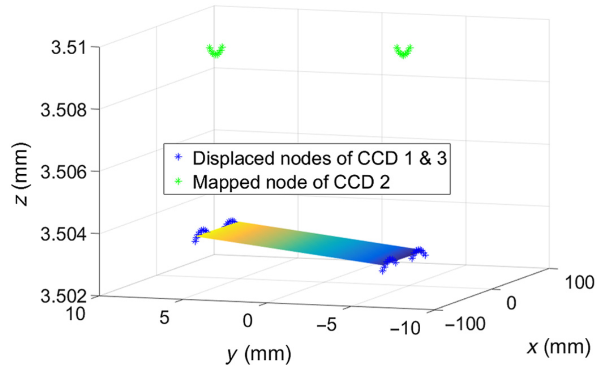

Fig. 9 Co-planarity error prediction results.

Table 1 Parameters of the fitted planes.

Parameters	a	b	c	d
Mirror plane	-5.84×10^{-6}	−0.7071	−0.7071	−18.0277
Imaging plane	-3.88×10^{-7}	6.02×10^{-5}	−1	3.5034

between the mapped nodes of CCD 2 and the fitted plane were calculated to obtain the co-planarity error. The parameters of the fitted planes are summarized in Table 1. The RMS value of the distances is 0.0062 mm.

The upper nodes of CCD 1 and 3 and the upper mapped nodes of CCD 2 (which were obtained by mapping the upper fitting nodes of CCD 2) as shown in Fig. 5 were used to predict the along-track position error. As shown in Fig. 10, the upper nodes of CCD 1 and 3 were used for line fitting, and the distances between the upper mapped nodes of CCD 2 and the fitted line were calculated. The line fitting results are shown in Table 2. The R^2 value of the line fit is 0.91. The RMS value of the distances is 0.00608 mm.

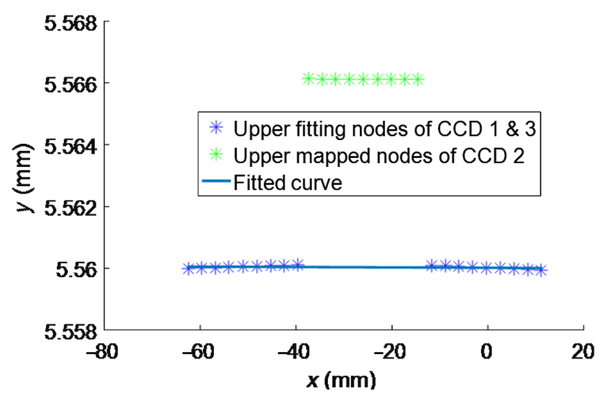

Fig. 10 Line fitting results.

Table 2 Line fitting results.

Parameters	a_l	b_l
Upper line	-6.37×10^{-7}	5.56

For the lap error calculation, the average of the displacements in X direction of each CCD is calculated and the relative distance changes are calculated according to Eq. (22). The lap error between CCD 1 and 2 is -0.0048 mm. The lap error between CCD 2 and 3 is -0.0046 mm.

5 Stability Experiment

To prove that the FPA design meets the mechanical and thermal stability requirements, three FPAs were tested and measured.

5.1 *Optical Bench Layout for Measurements*

The optical bench was set up both for the FPA integration and measurement. As shown in Fig. 11, the optical bench consists of a high precision three axes air bearing platform, light source, lens, camera, computer, and reference reticle. The performance of the platform is summarized in Table 3. The light source, lens, and camera are mounted on the linear platform, which moves along the three axes to achieve three-dimensional non-contact positional measurement. The platform also allows immunity from vibration transmitted by the floor.

The position of CCD was represented by measuring the position of the four patterns on each CCD as shown in Fig. 12. The measuring process includes the following.

(1) The FPA was installed on the optical bench using the prism of FPA. The X, Y, and Z axes of the platform are corresponding to the cross-track, along-track, and optical-axis direction, respectively, which are the same with the coordinate of FPA model.
(2) Moving the linear stage for the superposition and focalization of the reticle at the position of the pattern under inspection.

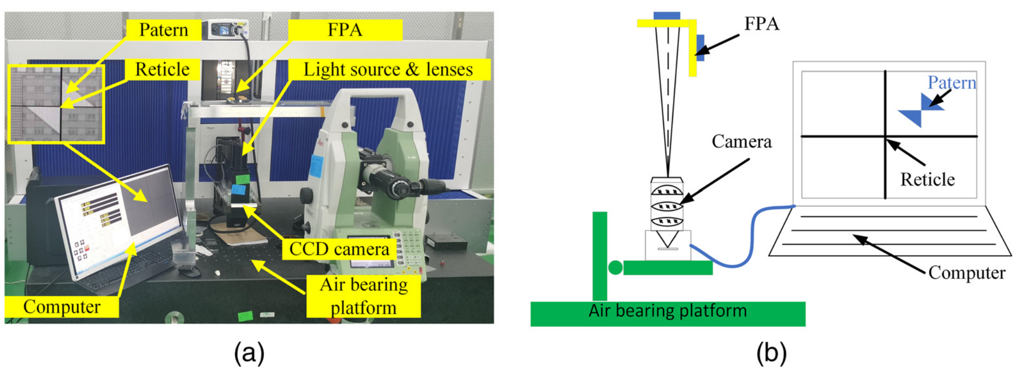

Fig. 11 Optical bench layout: (a) device of the optical bench and (b) schematic of the optical bench.

Table 3 Three axes air bearing platform features.

Translation capabilities (mm)	Resolution (μm)	Accuracy (μm)
X: 1000, Y: 400, and Z: 300	≤ 0.1	≤ 1

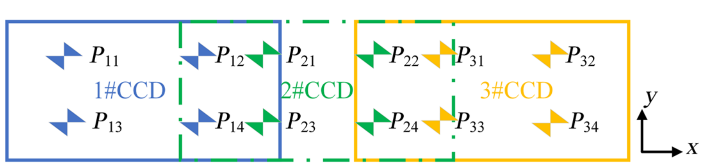

Fig. 12 Patterns on each CCD.

(3) Recording the coordinate position of the pattern.
(4) Calculating the relative positions of each CCDs.

The superposition and focalization of the reticle at the position of P_{11} was conducted first and this position value was set as (0, 0, 0) in the computer. Then the positions of the other patterns were measured, respectively. For the X and Y directional position measurements are determined by the superposition of the reticle and the pattern, the measurement accuracy in these directions can reach a high accuracy 1 μm with the high-precision resolution of the platform. However, the position measurement in Z direction is determined by the focalization of the pattern (the clarity of the pattern's image). Due to the influence of human vision error and liquid crystal display error factors, the position measurement accuracy in Z direction is 5 μm. However, it is difficult to measure the alignment errors of the FPA under the thermal or vibration experiment. The comparison of the proposed method and experimental measurements cannot be done at present.

5.2 *Experimental Results*

After the assembly of the focal plane, the vibration and thermal cycling test were performed in sequence, as shown in Fig. 13. Moreover, the measurement of FPAs was performed after the vibration and thermal cycling test, respectively, to obtain the positional changes of the CCDs. The FPAs were subjected to random vibration ($5g$ RMS) in three axes, respectively, for 90 s in vibration test. The duration of the thermal cycle ($-10°C/40°C$) was 60 min for 6 cycles.

The measurement data of the three FPAs in three-axis are illustrated in Appendix B. For the lap dimension stability analysis, the relative positions of the CCDs in X direction are calculated as

$$D_{12} = X_{P21} - X_{P12}, \quad D_{32} = X_{P31} - X_{P22}, \tag{23}$$

where D_{12} and D_{32} are the X directional distance between CCD 1 and 2 and CCD 2 and 3, respectively. X_{Pij} respects the X directional position of P_{ij} and $1 \leq i$ and $j \leq 3$.

Then the changes of distance in X direction were calculated after vibration test and thermal cycling experiment. Table 4 summarized the corresponding results in X direction.

The RMS and PV value of the dimension stability of the three FPAs in the three directions is summarized in Table 5, which shows the FPAs have a good mechanical and thermal stability.

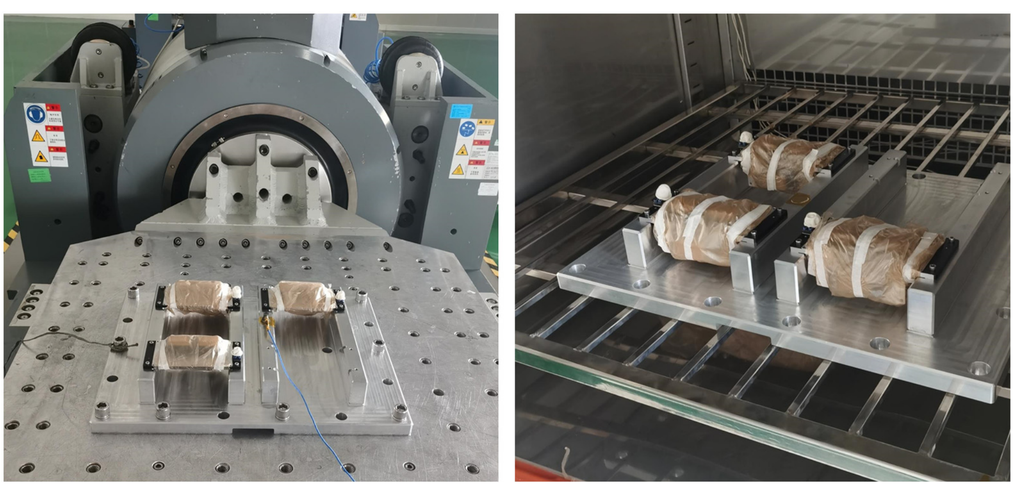

(a) (b)

Fig. 13 (a) Vibration and (b) thermal cycling test.

Table 4 Distances and changes in X direction (mm).

FPA	Stage	D_{12}	Change	D_{32}	Change
1#	Assembly	10.933	0	10.736	0
	Vibration	10.935	0.002	10.734	−0.002
	Thermal	10.936	0.001	10.733	−0.001
2#	Assembly	10.879	0	10.600	
	Vibration	10.879	0	10.598	−0.002
	Thermal	10.876	−0.003	10.600	0.002
3#	Assembly	10.664	0	10.853	0
	Vibration	10.666	0.002	10.853	0
	Thermal	10.662	−0.004	10.857	0.004

Table 5 Dimension stability (μm).

Direction	RMS	PV
Lap	2.3	4
Along-track	0.9	2
Co-planar	3.2	5

6 Conclusion

The main requirement of the spaceborne FPA system is positional stability of individual CCDs under operational and experimental conditions. In order to prove that the FPA designs meet the requirements, both analytical and experimental methods are presented in this paper. The design of FPA with optical splicing system is also discussed considering the material selection and thermo-structure behavior to ensure mechanical and thermal stability.

A general and systematic methodology has been proposed to combine alignment error calculation with FEA results. The FEA of the FPA was performed and the alignment errors were calculated due to thermal and gravity loadings. The results showed that the FPA design is within the allowable alignment displacement specification required for satisfactory spaceborne camera operation. One of the key properties of the alignment error calculation is that the FEA output results are used to postprocess, which is easy to be performed while ensuring relatively high accuracy.

The optical bench set up both for the assembly and measurement of focal plane was introduced. Vibration and thermal cycling test of three FPAs were conducted to verify the mechanical and thermal stability. The results showed that the FPA provides high relative stability over the experimental conditions. The postprocessing method proposed in this paper can be applied to transient analysis. The thermal field of the FPA under operating is obtained through thermal analysis, and then the thermal load is mapped to the finite-element node for thermal deformation analysis. After obtaining the deformed structure, the postprocessing method proposed in this paper can be used for alignment analysis. In the next step of research, we will investigate the alignment error measurement method of FPA under the thermal experiment.

7 Appendix A

For $V = [v_1, v_2, v_3] \in R^{3*3}$ is orthogonal matrix, then $X = [a, b, c]^{\mathrm{T}}$ can be written as

$$X = k_1 v_1 + k_2 v_2 + k_3 v_3, \tag{24}$$

with the constraint $\|X\| = 1$.

By substituting Eq. (15) into Eq. (14), we obtain

$$\begin{aligned}
\min\|AX\| &= \min(X^{\mathrm{T}}A^{\mathrm{T}}AX)\\
&= \min\left(X^{\mathrm{T}}V\begin{bmatrix}\sigma_1^2 & & \\ & \sigma_2^2 & \\ & & \sigma_3^2\end{bmatrix}V^{\mathrm{T}}X\right)\\
&= \min\left(X^{\mathrm{T}}[v_1 v_2 v_3]\begin{bmatrix}\sigma_1^2 & & \\ & \sigma_2^2 & \\ & & \sigma_3^2\end{bmatrix}\begin{bmatrix}v_1^{\mathrm{T}}\\ v_2^{\mathrm{T}}\\ v_3^{\mathrm{T}}\end{bmatrix}X\right)\\
&= \min\left(X^{\mathrm{T}}\begin{bmatrix}\sigma_1^2 v_1 v_1^{\mathrm{T}} & & \\ & \sigma_2^2 v_2 v_2^{\mathrm{T}} & \\ & & \sigma_3^2 v_3 v_3^{\mathrm{T}}\end{bmatrix}X\right)\\
&= \min\left([k_1 v_1 k_2 v_2 k_3 v_3]\begin{bmatrix}\sigma_1^2 & & \\ & \sigma_2^2 & \\ & & \sigma_3^2\end{bmatrix}\begin{bmatrix}k_1 v_1^{\mathrm{T}}\\ k_2 v_2^{\mathrm{T}}\\ k_3 v_n^{\mathrm{T}}\end{bmatrix}\right)\\
&= \min(k_1^2\sigma_1^2 + k_2^2\sigma_2^2 + k_3^2\sigma_3^2). \qquad (25)
\end{aligned}$$

Since $\sigma_1^2 \geq \sigma_2^2 \geq \sigma_3^2$, the minimum value of $\|AX\|$ is obtained when $k_3 = 1$ and $k_1 = k_2 = 0$. Then

$$\min\|AX\| = \sigma_3^2. \qquad (26)$$

According to Eq. (24), $X = v_3$, which indicates that X can be captured by the singular vector corresponding to the smallest singular value of A.

8 Appendix B

The measurement data of the three FPAs after assembly, vibration and thermal cycling in $X - Y$ directions are shown in Table 6, and the measurement data in Z directions are shown in Table 7.

Table 6 $X - Y$ measurement data (nm).

		X direction						Y direction					
		CCD 1		CCD 2		CCD 3		CCD 1		CCD 2		CCD 3	
FPA	Stage	P_{11}	P_{12}	P_{21}	P_{22}	P_{31}	P_{32}	P_{11}	P_{12}	P_{21}	P_{22}	P_{31}	P_{32}
1#	Assembly	0	14.614	25.547	40.161	50.897	65.511	0	−0.001	0	0	−0.001	−0.001
	Vibration	0	14.614	25.549	40.162	50.896	65.51	0	0	0.001	0	0	0
	Thermal	0	14.613	25.549	40.163	50.896	65.51	0	0	0	0	0	0.001
2#	Assembly	0	14.613	25.492	40.104	50.704	65.317	0	−0.001	0	0	−0.001	−0.001
	Vibration	0	14.613	25.492	40.105	50.703	65.317	0	0	0.001	0.001	0.001	0.001
	Thermal	0	14.613	25.489	40.101	50.701	65.317	0	0	0	0	−0.001	0
3#	Assembly	0	14.614	25.278	39.892	50.745	65.359	0	0.001	0	0	0	0.001
	Vibration	0	14.613	25.279	39.894	50.747	65.361	0	0.001	0	0	0	0.001
	Thermal	0	14.614	25.276	39.89	50.747	65.361	0	0	−0.002	−0.002	−0.002	−0.002

Table 7 Z measurement data (mm).

		CCD 1						CCD 2				CCD 3	
FPA	Stage	P_{11}	P_{12}	P_{21}	P_{22}	P_{31}	P_{32}	P_{11}	P_{12}	P_{21}	P_{22}	P_{31}	P_{32}
1#	Assembly	0	0	0.005	0	0	0	0.005	0	0	0.01	0	0.005
	Vibration	0	0	0.005	0	0	0	0.005	0	0	0.005	0	0
	Thermal	0	0	0.005	0	0.005	0	0	−0.005	0	0.005	−0.005	0
2#	Assembly	0	0	0	0	−0.005	0	0	0	−0.005	−0.005	−0.005	−0.005
	Vibration	0	0	0	0	−0.005	−0.005	0	0	−0.005	−0.005	−0.005	−0.005
	Thermal	0	0	0	0	0	−0.005	0	0	−0.005	−0.005	−0.005	−0.005
3#	Assembly	0	0	0.005	0	0.005	0.005	0	0	0	0.005	0	0
	Vibration	0	0	0.005	0	0	0.005	0	0	0	0.005	0	0
	Thermal	0	0	0.005	0	0.005	0.005	0	0	0	0	0	0

Acknowledgments

The authors would like to thank the financial support of the National Key Research and Development Program from Ministry of Science and Technology of the People's Republic of China (No. 2016YFB0500904). The authors declare no conflicts of interest.

References

1. G. A. Luppino, J. L. Tonry, and C. W. Stubbs, "CCD mosaics—past, present, and future: a review," *Proc. SPIE* **3355**, 469–476 (1998).
2. Y. Li et al., "Detailed analysis of the HIRISE FPA," *Key Eng. Mater.* **552**, 64–68 (2013).
3. K. J. Malone et al., "Landsat 9 OLI 2 focal plane subsystem: design, performance, and status," *Proc. SPIE* **10402**, 1040206 (2017).
4. K. Lindahl et al., "Summary of the operational land imager focal plane array for the Landsat Data Continuity Mission," *Proc. SPIE* **8155**, 81550Y (2011).
5. H. Lei et al., "Imaging characteristics of an optical butting camera," *Proc. SPIE* **7654**(3), 765415 (2010).
6. P. Pranyies et al., "SiC focal plane assembly for the Pleiades HR Satellite," *Proc. SPIE* **5570**, 568–576 (2004).
7. R. L. Goff, "Focal plane AIT sequence: evolution from HRG-Spot 5 to Pleiades HR," ESA Special Publications 621 (2006).
8. P. A. Scowen et al., "Large focal plane arrays for future missions," Astro2010 Technology White Paper, submitted to New Worlds, New Horizons in Astronomy and Astrophysics (2009).
9. A. Laborie, et al., "The Gaia focal plane," *Proc. SPIE* **6690**, 66900A (2007).
10. D. Hamill, "Thermal effects on alignment stability of electro optical systems," Master of Engineering, College of Engineering, Teas Tech University, Lubbock, Texas (2005).
11. R. D. Cook et al., *Concepts and Applications of Finite Element Analysis*, 4th ed., John Wiley & Sons, New York (2002).
12. H. A. Macewen et al., "Focal plane mechanical design of the NISP/Euclid instrument," *Proc. SPIE* **9904**, 99042V (2016).
13. J. A. Sultana and M. B. O'Neill, "Design, analysis, and testing of a CCD array mounting structure," *Proc. SPIE* **1532**, 27–38 (1991).
14. J. D. Johnston et al., "Integrated modeling activities for the James Webb Space Telescope: structural-thermal-optical analysis," *Proc. SPIE* **5487**, 600–610 (2004).

15. Z.-P. Xue et al., "Integrated optomechanical analyses and experimental verification for a thermal system of an aerial camera," *Appl. Opt.* **58**(26), 6996–7005 (2019).
16. V. Genberg and G. Michels, "Integrated optomechanical STOP analysis linking Nastran to Zemax, CODEV, and OSLO with SigFit," in *White Paper*, Sigmadyne. Inc. (2017).
17. P. Edward, "The use of decomposition SVD to approximate a surface," in *Environ. Eng. Int. Conf.* (2017).
18. D. Zermas, I. Izzat, and N. Papanikolopoulos, "Fast segmentation of 3D point clouds: a paradigm on LiDAR data for autonomous vehicle applications," in *IEEE Int. Conf. Rob. and Autom. (ICRA)*, IEEE, pp. 5067–5073 (2017).

Zhi-Peng Xue received his PhD from the University of Chinese Academy of Sciences, Beijing, China, in 2015. He is an assistant research fellow at Changchun Institute of Optics of Fine Mechanics and Physics at Chinese Academy of Sciences. He also served at the Chang Guang Satellite Technology Company, Changchun, China and joined several projects, including UAV system, aerial camera, spaceborne camera, and satellite (Jilin-1 Gaofen-03). His research area is optomechanical integrated analysis and optimization.

Sheng Wang received his master's degree from Jilin University, Changchun, China, in 2017. He is currently an engineer at Chang Guang Satellite Technology Company, Changchun, China. He is in charge of the development of optomechanical structure for the Jilin-1 Gaofen-03. He specializes in lightweight structure design and structural vibration.

Shan-Shan Cong received her master's degree from Changchun University of Science and Technology, Changchun, China, in 2008. She is an associate research fellow at Chang Guang Satellite Technology Company, Changchun, China. She is in charge of some projects for optomechanical system design, assembly, and measurement including Jilin-1 Kuanfu-01 and Gaofen-03 satellite.

Lei Zhang received his PhD from Changchun Institute of Optics, Fine Mechanics and Physics, Chinese Academy of Sciences, Changchun, China, in 2008. He was assigned as a professor of Chinese Academy of Sciences in 2019. He is currently a vice general manager at Chang Guang Satellite Technology Company, Changchun, China. He is in charge of the development of Jilin-1 Kuanfu-01 and 01B satellites and 20 kg microsatellites. His research area includes optical remote sensing satellite and aerospace structure.

Mei-Jiao Sun received her master's degree from Changchun University of Science and Technology, Changchun, China, in 2017. She is an engineer at Chang Guang Satellite Technology Company, Changchun, China. She is incharge of some projects for optical assembly and measurement.

Chun-Yu Zhu received his undergraduate degree from Changchun University of Technology, Changchun, China, in 2009. He is an engineer at Chang Guang Satellite Technology Company, Changchun, China. He is in charge of some projects for focal plane alignment.

Chang Liu received his master's degree from Beihang University, Beijing, China, in 2018. He is currently an engineer at Chang Guang Satellite Technology Company, Changchun, China. He is in charge of some projects for space mirror development.

Hang Liu received his master's degree from Jilin University, Changchun, China, in 2018. He is currently an engineer at Chang Guang Satellite Technology Company, Changchun, China. His research area is developing lightweight, stable designs for space mirrors.